ChemComm

COMMUNICATION

View Article Online
View Journal

Cite this: DOI: 10.1039/d5cc05610a

Received 29th September 2025,
Accepted 17th April 2026

DOI: 10.1039/d5cc05610a

rsc.li/chemcomm

Chirality-tuned magnetic susceptibility of chiral mesostructured cobalt oxide films

Liuliu He, Wenjun Zhu, Yang Gao, Quanzheng Deng and Yingying Duan *

Chiral mesostructured cobalt oxide films (CMCFs) are synthesized hydrothermally using amino acids as symmetry-breaking agents. Their chiral orientation is reversibly controlled by pH, which in turn modulates the magnetic susceptibility, an effect that is hypothetically attributed to the chirality-induced spin selectivity (CISS) effect.

In condensed matter systems, complex interplays exist among electron spin, charge, orbital and lattice degrees of freedom.[1,2] These interactions give rise to exotic physical properties in materials, including optical, electric, and magnetic characteristics. With advancing device technologies, researchers have developed various approaches to engineer material magnetism beyond intrinsic behaviour, such as external field manipulation,[3–5] interface engineering,[6–8] and internal modifications through doping[9–11] and defect formation.[12,13] However, these magnetic manipulations remain constrained by the requirement of external magnetic fields or specific chemical compositions. Recently, studies have revealed that incorporating chiral structures into materials can modulate magnetism through spin manipulation *via* asymmetric spin–orbit coupling.[14–16]

The magnetism of cobalt oxides (Co_xO_y) primarily originates from their complex valence state variations and crystal structures.[17] This enables cobalt to exist in various spin states in its oxide forms, including low, high, and intermediate spin configurations.[18] The integration of cobalt oxides' complex spin characteristics with chiral structures presents promising opportunities for studying structure-tunable magnetism.

In this work, chiral mesostructured cobalt oxide films (CMCFs) were fabricated on quartz substrates *via* a hydrothermal method using a homogeneous solution containing histidine, cobalt nitrate, PVP, ammonia, and deionized water at 180 °C (Fig. S1–S4, SI). The quartz substrates were pretreated with potassium permanganate to generate active sites for effective interaction with amino acids.[19] Enantiomeric histidine was selected as both a symmetry-breaking and structure-directing agent due to its effective chelation with cobalt ions. PVP served as a dispersant, while ammonia provided OH^- ions to establish a high-pH environment conducive to cobalt precipitation and cobalt hydroxide film formation. After calcination, CMCFs without organic residues were obtained (Fig. S5, SI). Samples prepared with D- and L-histidine are designated as D- and L-CMCFs, respectively. CMCFs synthesized at pH values of 10 and 11 are labelled as 10D-, 10L-, 11D-, and 11L-CMCFs, respectively.

The crystalline structure of the CMCFs was characterized by grazing incidence X-ray diffraction (GIA-XRD). As shown in Fig. 1, both 10D- and 11D-CMCFs exhibit identical XRD patterns. The diffraction reflections indicate that the CMCFs are composed of two cobalt oxide phases. The XPS spectrum confirms mixed valence states of cobalt oxide (Fig. S6, SI). The reflections of (220), (311), (222) and (440) match well with the cubic phase of Co_3O_4 (space group $Fd\bar{3}m$, lattice parameter a = 9.10 Å), as simulated using VESTA. In addition, the (111) reflection can be indexed to the cubic phase of CoO_2 (space group $Fd\bar{3}m$, a = 7.85 Å). No additional diffraction peaks corresponding to other crystalline byproducts are observed. Notably, the intensity of the (311) reflection is significantly

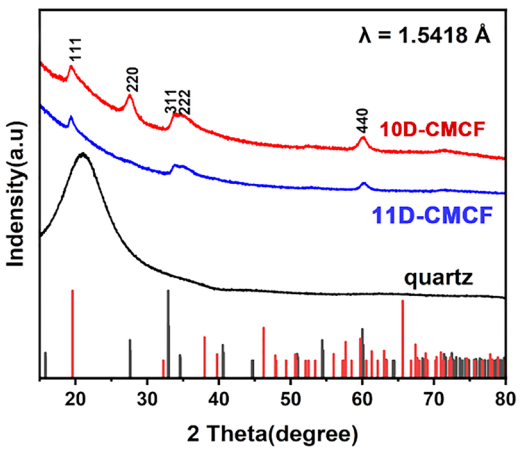

Fig. 1 The GIA-XRD patterns of the 10D- and 11D-CMCFs.

School of Chemical Science and Engineering, Tongji University, 1239 Siping Road, Shanghai, 200092, P. R. China. E-mail: yyduan@tongji.edu.cn

lower than that typically observed in the bulk material, whereas the (222) reflection is markedly enhanced, suggesting a preferred crystallographic orientation growth along the (222) direction in the CMCFs. Consistent with this, antipodal CMCFs also display identical XRD patterns (Fig. S7, SI).

As illustrated in Fig. 2, the CMCFs appear semi-transparent with brown colour and exhibit a smooth and uniform surface morphology (Fig. S8, SI). The 10D-CMCFs are composed of densely packed nanoplate arrays vertically aligned on quartz substrates, with individual nanoplates having a thickness of ~10 nm (Fig. 2a) and a height of ~1.5 μm (Fig. S9, SI). These nanoplates are arranged in an oriented manner, collectively giving rise to a chiral architecture. When the pH of the reaction solution is increased to 11, the resulting 11D-CMCFs exhibit a more sparsely arranged nanoplate morphology, in which the chiral character becomes less evident. Nevertheless, the presence of bent edges in the nanostructures indirectly implies the existence of such twisted geometries. Antipodal CMCFs show similar morphological profiles but with opposite chiral directions, as confirmed by optical activity (OA) (Fig. S10, SI).

The chirality of the CMCFs was unambiguously confirmed by measuring their OA using ultraviolet-visible (UV-Vis) and circular dichroism (CD) spectroscopy. Fig. 2c_1 and d_1 present the transmitted UV-Vis and mirror-image CD spectra of the antipodal 10-CMCFs and 11-CMCFs, respectively. Taking 10D-CMCF as an example, a broad band is observed in the UV-Vis spectrum from 250 to 800 nm, along with an intense CD peak near 360 nm. According to the characteristic mechanism,[20] the transmitted CD spectrum contains contributions from both absorption- and scattering-based OA. After infiltration with water, the CD signal of the antipodal 10-CMCFs shows significant attenuation (Fig. S11, SI), indicating a positive scattering-based signal arising from a left-handed structure. The measurement of CD at varying rotation degrees confirms the absence of artifacts, such as linear dichroism (Fig. S12, SI). Furthermore, diffuse-reflection UV-Vis (DRUV-Vis) and CD (DRCD) spectroscopy with a white background were employed to illustrate the absorption-based OA (Fig. 2c_2 and d_2). The DRCD spectrum of the 10D-CMCFs exhibits a positive band at 500–800 nm and a negative band at around 300 nm. These signals may originate from d–d transitions associated with a positive chiral structure and electron transitions from the valence band to the conduction band with a negative chiral structure, respectively. The 10L-CMCFs exhibited mirror imaged CD signals, confirming the opposite chiral orientation relative to its antipodal counterpart. Interestingly, the transmitted CD spectrum of the 11D-CMCFs exhibits a positive broad band in the visible region, indicating a scattering-based OA with the same orientation. However, the DRCD spectrum of the 11D-CMCFs shows an opposite CD signal at 300 nm with a positive chiral structure, which is inverted relative to that of 10D-CMCFs. Therefore, it is deduced that the dominant chirality of the 10-CMCFs and 11-CMCFs may be opposite.

Fig. 3a_1 and b_1 present the *M–H* curves measured at 300 K with the magnetic field applied perpendicular to the sample surface. Over the field range of −3 to 3 T, the samples overall exhibit antiferromagnetic behaviour at room temperature, while a weak ferrimagnetic-like response is observed under low external magnetic fields. The magnetic susceptibility (χ) of the 10D-CMCFs (1.481×10^{-6} emu g^{-1} Oe^{-1}) was found to be higher than that of the 10L-CMCFs (1.196×10^{-6} emu g^{-1} Oe^{-1}) with increasing magnetic field. In contrast, for the 11-CMCFs

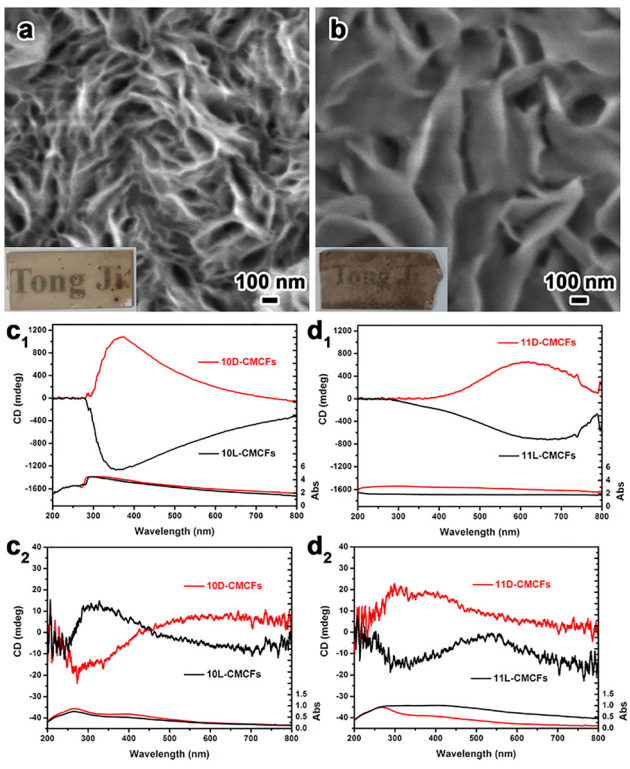

Fig. 2 (a) and (b) SEM images of the 10D- and 11D-CMCFs, respectively. Transmitted CD and UV-Vis spectra of the 10D- (c_1) and 11D-CMCFs (d_1). DRCD and DRUV-Vis spectra of the 10D- (c_2) and 11D-CMCFs (d_2) measured with a white background.

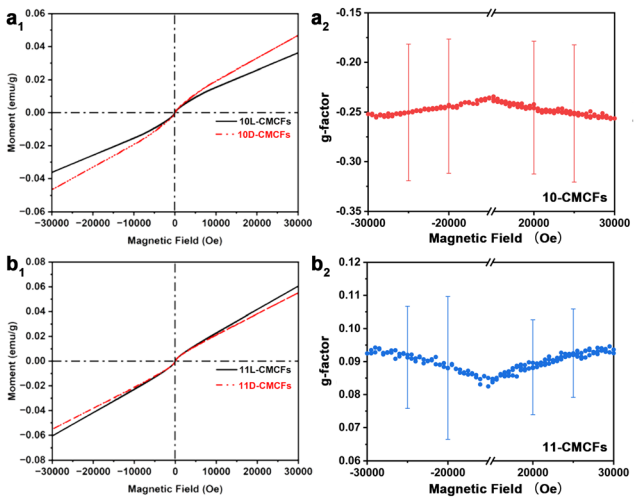

Fig. 3 *M–H* curves and magnetization *g*-factors of antipodal (a_1 and a_2) 10-CMCFs and (b_1 and b_2) 11-CMCFs.

with opposite chiral structures, the magnetic susceptibility of the 11L-CMCFs (1.948×10^{-6} emu g^{-1} Oe^{-1}) was observed to be higher than that of the 11D-CMCFs (1.769×10^{-6} emu g^{-1} Oe^{-1}) with increasing magnetic field strength. The consistency and reproducibility of the chiral anisotropy of magnetization were confirmed for four additional pairs of antipodal films fabricated under identical preparation parameters (Fig. S13, SI). Furthermore, we quantified this chiral anisotropy using a g-factor defined as $g = 2(M_L - M_D)/(M_L + M_D)$, where M_L and M_D represent the magnetization of the L- and D-CMCFs, respectively (Fig. S14, SI). As shown in Fig. $3a_2$ and b_2, the average g-factors of the 10-CMCFs are consistently negative, while those of the 11-CMCFs are consistently positive across all batches. These results show a consistent correlation between the presence of a negative CD signal and an enhanced magnetic susceptibility. Given the identical phase composition evidenced by XRD and XPS (Fig. S15, SI), the variation in magnetic susceptibility is associated with the chiral orientation, rather than with differences in the proportions of the constituent magnetic phases.

To elucidate the mechanism underlying the chirality-tuned magnetic properties, we conducted a systematic magnetic circular dichroism (MCD) study (MCD = $CD_{B\neq0} - CD_{B=0}$), which is particularly sensitive to spin-polarized states near the band edge (Fig. S16 and S17, SI).[21] Fig. 4 displays the MCD spectra of the CMCFs under a magnetic field of ±1.5 T at 293 K (obtained from CD spectra under a magnetic field of ±1.5 T, Fig. S18). The CD spectra of the 10D-CMCFs (Fig. 4a) display a positive signal centered at 420 nm, corresponding to

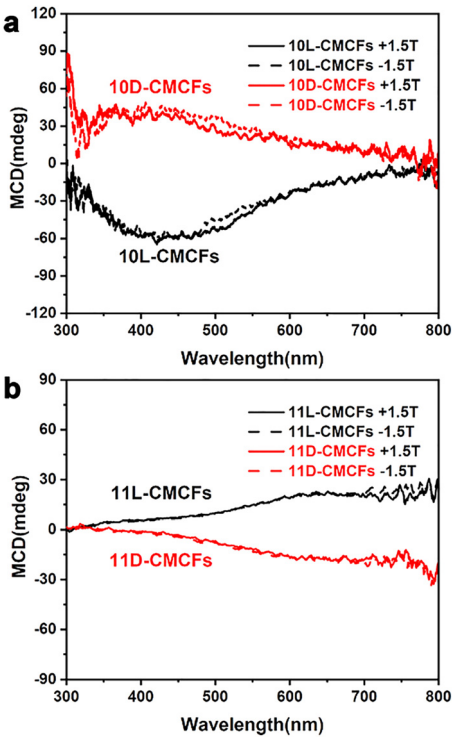

Fig. 4 MCD spectra of antipodal (a) 10-CMCFs and (b) 11-CMCFs measured under an external magnetic field of ± 1.5 T.

electron transitions from the valence band to the conduction band. The deviation from the DRCD spectra may be attributed to the complete absorption of left- and right-circularly polarized light in the ultraviolet region. Nevertheless, the MCD signals remain consistent under parallel and antiparallel external magnetic fields, indicating that the response is independent of the magnetic field direction. Mirror-image MCD signals with opposite signs were observed for the 10L-CMCFs. In contrast, the MCD spectra of the 11D- and 11L-CMCFs (Fig. 4b) exhibit signals opposite to those of their antipodal 10-CMCF counterparts, consistent with the optical activity (OA) results. Furthermore, achiral cobalt oxide thin films (ACFs) exhibit no CD signal in circular dichroism spectroscopy, and their magneto-optical circular dichroism (MCD) spectra show almost no CD signal under both positive and negative 1.5 T magnetic fields (Fig. S19, SI). These findings suggest opposite spin polarization in CMCFs with opposing chiral structures. The structural and chemical consistency between the powder and thin film, as confirmed by SEM, XRD, and CD measurements, ensures that the oxygen vacancies in the powder share the same local coordination environment and thus the same EPR characteristics as those in the thin film (Fig. S20, SI). The electron paramagnetic resonance (EPR) results of the powder sample offer indirect evidence suggesting the presence of spin-polarized centers in the corresponding chiral films (Fig. S21, SI).

Based on the experimental results and previous theoretical frameworks,[22,23] we propose a plausible mechanism for the chirality-dependent enhancement of magnetic susceptibility in CMCFs. The weak ferrimagnetism in CMCFs originates from uncompensated antiferromagnetic coupling among high-spin Co^{2+} ions on the frustrated tetrahedral sublattice, while low-spin Co^{3+} ions remain magnetically inactive. The breaking of inversion symmetry in CMCFs introduces a chiral potential. Electron motion within this potential generates a chirality-induced magnetic field, which acts on the magnetic moments of electrons and leads to chirality-induced spin polarization – a phenomenon known as the chirality-induced spin selectivity (CISS) effect. Hypothetically, in CMCFs featuring a negative CD signal, a parallel alignment between the intrinsic and chirality-induced spin polarizations may occur, and this alignment correlates with an enhanced magnetic susceptibility. Conversely, in CMCFs with a positive CD signal, an antiparallel alignment of these spin polarizations is hypothesized, which correlates with a reduced magnetic susceptibility. We propose this as a tentative mechanism based on the observed spin polarization evidence, while recognizing that a definitive causal explanation awaits a more complete understanding of the CISS effect.

In CMCFs featuring a negative chiral structure, a parallel alignment is observed between the intrinsic and chirality-induced spin polarizations, and this alignment correlates with an enhanced magnetic susceptibility. Conversely, in CMCFs with a positive chiral structure, an antiparallel alignment of these spin polarizations is found, which correlates with a reduced magnetic susceptibility.

In summary, chiral mesostructured cobalt oxide films were successfully synthesized *via* a facile chiral molecule-assisted

hydrothermal route. The observed chirality-mediated tuning of magnetic properties represents a significant advancement in the field of chiral materials. This work provides a novel strategy for modulating magnetism through structural chirality.

Conflicts of interest

There are no conflicts to declare.

Data availability

The data supporting this article have been included as part of the supplementary information (SI). Supplementary information is available. See DOI: https://doi.org/10.1039/d5cc05610a.

Acknowledgements

This work was supported by the National Natural Science Foundation of China (22375151, Y. D.).

References

1 S. V. Streltsov and D. I. Khomskiĭ, *Phys.-Usp.*, 2017, **60**, 1121–1146.
2 Y. Tang, F. Feng, G. Xu, S. Qin, X. Ouyang, L. Yao and X. Wang, *Sci. China Mater.*, 2024, **67**, 3049–3082.
3 B. Huang, G. Clark, D. R. Klein, D. MacNeill, E. Navarro-Moratalla, K. L. Seyler, N. Wilson, M. A. McGuire, D. H. Cobden, D. Xiao, W. Yao, P. Jarillo-Herrero and X. Xu, *Nat. Nanotechnol.*, 2018, **13**, 544–548.
4 T. Song, Z. Fei, M. Yankowitz, Z. Lin, Q. Jiang, K. Hwangbo, Q. Zhang, B. Sun, T. Taniguchi, K. Watanabe, M. A. McGuire, D. Graf, T. Cao, J.-H. Chu, D. H. Cobden, C. R. Dean, D. Xiao and X. Xu, *Nat. Mater.*, 2019, **18**, 1298–1302.
5 J. Chen, X. Xie, X. Oyang, S. Li, J. He, Z. Liu, J.-T. Wang and Y. Liu, *Small*, 2024, **20**, 2404346.
6 J. Wan, S. D. Lacey, J. Dai, W. Bao, M. S. Fuhrer and L. Hu, *Chem. Soc. Rev.*, 2016, **45**, 6742–6765.
7 M. Rajapakse, B. Karki, U. O. Abu, S. Pishgar, M. R. K. Musa, S. M. S. Riyadh, M. Yu, G. Sumanasekera and J. B. Jasinski, *npj 2D Mater. Appl.*, 2021, **5**, 30.
8 L. Zhang, C. Tang, S. Sanvito, Y. Gu and A. Du, *ACS Appl. Mater. Interfaces*, 2022, **14**, 1800–1806.
9 L. Chen, X. Yang, F. Yang, J. Zhao, J. Misuraca, P. Xiong and S. von Molnár, *Nano Lett.*, 2011, **11**, 2584–2589.
10 Y. Wang, S. Li and J. Yi, *Sci. Rep.*, 2016, **6**, 24153.
11 L. Tang, R. Xu, J. Tan, Y. Luo, J. Zou, Z. Zhang, R. Zhang, Y. Zhao, J. Lin, X. Zou, B. Liu and H.-M. Cheng, *Adv. Funct. Mater.*, 2021, **31**, 2006941.
12 B. Sainbileg, E. Batsaikhan and M. Hayashi, *RSC Adv.*, 2020, **10**, 42493–42501.
13 R. Wang, Y. Su, G. Yang, J. Zhang and S. Zhang, *Chem. Mater.*, 2020, **32**, 1545–1552.
14 G. Long, Y. Zhou, M. Zhang, R. Sabatini, A. Rasmita, L. Huang, G. Lakhwani and W. Gao, *Adv. Mater.*, 2019, **31**, 1807628.
15 M. Gao and W. Qin, *Adv. Opt. Mater.*, 2021, **9**, 2101201.
16 B. Zhang, J. Ai, Y. Duan, T. Bai, L. Han and S. Che, *Nano Res.*, 2024, **17**, 2019–2024.
17 S. Iravani and R. S. Varma, *Green Chem.*, 2020, **22**, 2643–2661.
18 Q. Dehaine, L. T. Tijsseling, H. J. Glass, T. Törmänen and A. R. Butcher, *Miner. Eng.*, 2021, **160**, 106656.
19 Y. Duan, L. Han, J. Zhang, S. Asahina, Z. Huang, L. Shi, B. Wang, Y. Cao, Y. Yao, L. Ma, C. Wang, R. K. Dukor, L. Sun, C. Jiang, Z. Tang, L. A. Nafie and S. Che, *Angew. Chem., Int. Ed.*, 2015, **54**, 15170–15175.
20 Y. Duan and S. Che, *Adv. Mater.*, 2023, **35**, 2205088.
21 T. Ji, S. Che and Y. Duan, *Acc. Mater. Res.*, 2023, **4**, 1057–1067.
22 B. P. Bloom, Y. Paltiel, R. Naaman and D. H. Waldeck, *Chem. Rev.*, 2024, **124**, 1950–1991.
23 Y. Zhou, T. Bai and Y. Duan, *Chem. Commun.*, 2023, **59**, 13207–13210.

